Nano Research 2015, 8(9): 2925–2934
DOI 10.1007/s12274-015-0797-8
Research Article
ISSN 1998-0124
CN 11-5974/O4

Facet selective etching of Au microcrystallites

Gangaiah Mettela and Giridhar U. Kulkarni (✉)

Thematic Unit of Excellence on Nanochemistry and Chemistry and Physics of Materials Unit, Jawaharlal Nehru Centre for Advanced Scientific Research (JNCASR), Jakkur P.O., Bangalore 560 064, India

Received: 23 March 2015
Revised: 9 April 2015
Accepted: 14 April 2015

KEYWORDS
gold,
microcrystallites,
facet selective etching,
capping

ABSTRACT

High-symmetry crystals exhibit isotropic properties. Inducing anisotropy, e.g., by facet selective etching, is considered implausible in face-centered cubic (FCC) metals, particularly gold, which, in addition to being an FCC, is noble. We report for the first time the facet selective etching of Au microcrystals obtained in the form of cuboctahedra and pentagonal rods from the thermolysis of a gold-organic precursor. The selective etching of {111} and {100} facets was achieved using a capping method in which tetraoctylammonium cations selectively cap the {111} facets while Br^- ions protect the {100} facets. The exposed facets are oxidized by O_2/Cl^-, yielding a variety of interesting geometries. The facet selective etching of the Au microcrystallites is governed only by the nature of the facets; the geometry of the microcystallite does not appear to play a significant role. The etched surfaces appear rough, but a closer examination reveals well-defined corrugations that are indexable to high *hkl* values. Such surfaces exhibit enhanced Raman activity.

1 Introduction

The crystal lattices of most metals are face-centered cubes (FCCs), which are highly symmetrical. Because of the large number of equal symmetry directions and facets, anisotropic etching is difficult in FCC metals, particularly noble metals. While anisotropic etching is well-known among low-symmetry semiconducting materials such as Si [1], Ge [2], and GaN [3], there are hardly any reports on metal crystals. In this study, we explored the anisotropic etching of Au microcrystals.

There are few reports on the anisotropic etching of the nanoparticles of noble metals. The etching of a nanoparticle facet depends on the surface energy (γ) of the facet, and the general trend is $\gamma_{(110)} > \gamma_{(100)} > \gamma_{(111)}$ [4]. Hence, it is expected that the {110}, {100}, and {111} facets exhibit high, medium, and low reactivities with a given etchant. However, there are counter effects due to the polarization [5], symmetry [6], and other parameters of adsorbed species that influence the facet selective etching of metal crystallites. For instance, Br^- anions bind preferentially to {100} facets [7], while quaternary cations bind to {111} facets [8]. The etching of a facet is a combined effect of the surface energy and the nature of the adsorbed species. In the absence of counter effects, etching proceeds in accordance

Address correspondence to kulkarni@jncasr.ac.in

with the surface energy. However, this often leads to irregular geometries (see Table S1 in the Electronic Supplementary Material (ESM)). The capping agent lowers the etchant interaction considerably with the adsorbent facets [9]. The strength of the etchant also plays an important role in guiding anisotropic etching. While isotropic etching occurs with a strong etchant (eg., HNO_3), no etching can occur if the etchant is too weak. Commonly used mild etchants for noble and semi-noble metals are H_2O_2 [10], CN^- [11], Fe(III) [12], Cu(II) [13, 14], Pb(II) [15], NH_3 [16] and O_2/Cl^- [7]. For instance, Pd cuboctahedra and octahedra were obtained from nanocubes by selective etching along the [111] direction using O_2/Cl^- as etchant while Br^- ions protected the {100} facets [7, 17]. Additionally, Yang et al. obtained a variety of geometries from an Ag octahedron by selectively etching the [100] facets using NH_4OH/H_2O_2, with PVP as the capping agent [16]. These studies produced interesting nanoparticle geometries without significantly altering the size. The etching of Au nanoparticles, unlike that of Ag and Pd, is difficult because Au is a noble metal. Jana et al. [18] reported the anisotropic etching of an Au spheroid to obtain spherical nanoparticles using CN^-. The electrochemical oxidation of Au crystals has also been reported [19, 20]. Pradeep et al. used $CuCl_2$ as an etchant for the anisotropic etching of Au nanorods, demonstrating the selective etching of the body and tip of the nanorods [21]. The Au nanorods were oxidized to form spherical nanoparticles using H_2O_2 [22, 23]. However, the nature and mechanism of the etched facets are unclear. All of the above examples pertain to particles with a size well below 300 nm. Fan et al. recently reported a versatile method for the selective etching of edges and {111} facets of Au nanocrystals with various shapes [24]. Face selective etching is useful not only to understand the nature of the facets but also to produce various shapes with nearly the same size. Because anisotropic etching does not alter the size of the nanoparticles, the obtained nanoparticles with different shapes are the ideal systems to study the shape-dependent properties.

We found it interesting to examine the anisotropic etching behavior of Au microcrystals in the form of Au polygonal plates grown in the laboratory, which are essentially single-crystalline with well-defined facets [25, 26]. An advantage of these materials is that the facet selective etching of the microplates and the crystallographic details of the etched facets can be visualized using common optical and electron microscopes, unlike nanoparticles, which require high-resolution transmission electron microscopy in order to be seen [27]. Thus far, a successful demonstration on large metal crystallites has not been reported. Although such studies can be conducted using bulk crystal surfaces, the facet selectivity is rather poor because of the inherent surface defects and dislocations [28]. We performed a systematic study on the selective etching of {100} and {111} facets in various types of Au microcrystals—cuboctahedra, hexagons, triangles, and pentagonal microrods—using Ag(I)- and Cu(II)-based etchants. The selective etching produced a variety of intermediates enclosed by highly corrugated surfaces that are indexable to high *hkl* values.

2 Experimental

2.1 Materials

Gold chloride ($HAuCl_4$), silver nitrate ($AgNO_3$), tetraoctylammonium bromide (ToABr), cupric chloride ($CuCl_2$), sodium chloride (NaCl), copper sulphate ($CuSO_4$), and toluene were used. All reagents were purchased from Spectrochem, India. The water used in this study was double-distilled and deionized. The Si substrates were cleaned with water, isopropyl alcohol, and toluene and dried in N_2 gas.

2.2 Synthesis of Au microcrystals

We added 100 μL of ToABr in toluene (50 mM) to 75 μL of $HAuCl_4$ (25 mM) and stirred for 5 min [25]. The bottom aqueous phase became colorless, and the top organic phase developed a red color. The obtained AuToABr complex had nearly the same melting point (~90 ℃) and decomposition temperature (~150 ℃) as ToABr. The organic layer was pipetted out, drop-coated on a Si substrate, and heated at 135 ℃ on a hotplate in air. After the Au microcrystals were grown, they were washed with toluene to remove any residual precursor and then dried with flowing nitrogen.

2.3 Preparation of AgToABr for the {100} facets etching

We added 25 μL of a $AgNO_3$ (25 mM) solution and 10 μL of HCl (110 mM) to a 200-μL ToABr (50 mM) solution and stirred for 5 min [29]. Excess ToABr was used to ensure the effective phase transfer of the Ag(I) to the organic layer. The obtained AgToABr complex was characterized using Fourier transform infrared spectroscopy, thermogravimetric analysis (TGA), and energy-dispersive spectroscopy (EDS) (see Figs. S1 and S10 in the ESM). The melting point and decomposition of the obtained AgToABr are nearly the same as those of ToABr and AuToABr. A 200-μL organic layer was removed and drop-coated on the as-prepared Au microcrystals and heated at 135 ˚C on a hotplate in air for 6 h. The samples were washed with toluene to remove the unreacted precursor and then dried under N_2 gas.

2.4 Etching of the {111} facets

The Au microcrystallites were dipped in 1 mL of a 0.5 M $CuCl_2$ solution and then heated at 60 ˚C in air. After 1 h, the solution was cooled to room temperature. The samples were removed, washed with plenty of water, dried in N_2 gas, and used for characterization.

2.5 Characterizations

Scanning electron microscopy (SEM) was performed using a Nova NanoSEM 600 equipment (FEI Co., The Netherlands). EDS mapping was performed using an EDAX Genesis V4.52 (USA) attached to the SEM column. Atomic force microscopy (AFM) experiments were conducted using a scanning probe microscope (Bruker Innova) with a nanodrive controller. Imaging was performed in the tapping mode. TGA was performed using a Mettler Toledo TG-850 in a N_2 atmosphere.

3 Results and discussion

3.1 Etching of {100} facets

Au microcrystals were prepared using a method reported recently in our laboratory [25]. In a typical synthesis of Au microcrystals, 100 μL of precursor obtained by the stabilization of $(AuCl_4)^-$ with ToABr was drop-coated on a glass or Si substrate and thermalized on a hotplate at 135 ˚C in air for 1 h.

At the thermolysis temperature of 60 ˚C, the growth of the Au microcrystals proceeded in the molten start of the precursor (AuToABr), while the decomposition started at ~150 ˚C (see Fig. S1 in the ESM). In the obtained product, two types of Au microcrystals were observed (see Fig. S2 in the ESM)—cuboctahedron derivatives and penta-twinned microrods—and the latter were less abundant. In the first category, in addition to the regular cuboctahedron, other analogous geometries—truncated octahedra [30], hexagons, and triangles—were observed (see Fig. S3 in the ESM). The crystallite size was in the range of 1–10 μm. Among these geometries, the regular cuboctahedron was our focus in this study. It is enclosed by 14 facets: eight triangular and six rectangular or square. As shown in Fig. 1(a), in the conformation of a cuboctahedron, the top and bottom facets are made of triangles, and the side facets are enclosed by six triangular and six rectangular or square facets, alternating [30, 31]. A typical view of the cuboctahedron particle is depicted in Fig. 1(a), where four triangular and three square facets are clearly observed, which are assigned to the {111} and {100} facets, respectively [31]. The edges are sharp, and the surface of each face is smooth, as shown in Fig. 1(b). To achieve anisotropic etching,

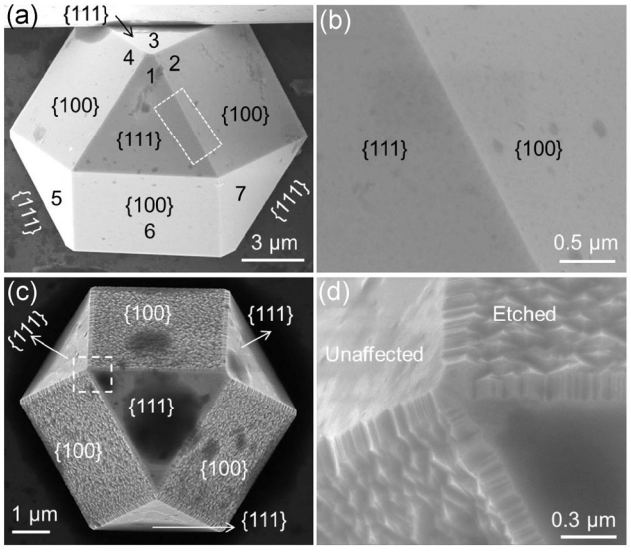

Figure 1 Typical SEM images of samples (a) and (b) as prepared and (c) and (d) after treatment with AgToABr for selective etching of the {100} facets.

various etchants, such as $FeCl_3$, NaCl, H_2O_2, ToABr, and AgToABr, were tested. Poor anisotropic etching was observed with $FeCl_3$, NaCl, H_2O_2 and ToABr (see Figs. S4–S6 in the ESM), whereas facet selective etching was achieved with AgToABr. Briefly, ~200 μL of the etching solution, AgToABr in toluene (see experimental section for the preparation), was added to the obtained microcrystals, and the thermolysis was continued at 135 ˚C.

The etching of the {100} facets occurred in molten AgToABr. The products obtained at various stages of the thermolysis were analyzed. An SEM image of a cuboctahedron obtained after 1 h of thermolysis is shown in Fig. 1(c). Interestingly, all the {100} facets were etched to the roughened surfaces, whereas the {111} facets appear unaffected in the magnified images shown in Fig. 1(d) and Fig. S7 (in the ESM) (see the low-magnification images shown in Fig. S8 (in the ESM)). This observation confirms the selective etching of the {100} facets by the AgToABr. In addition, the edges and corners were also roughened (Fig. 1(d)). We recall that selective etching of the {100} facet has been examined with Ag [16] and Pd nanocrystals [7] but not Au.

The continued etching of the {100} facet produced concave-type deepening as shown in Fig. 2(a); however, this disappeared during further etching, owing to the thermodynamic instability [27]. It appears that as the {100} facets were gradually etched, a variety of intermediates formed, and the {111} facets were unaffected (Figs. 2(a) and 2(b)). However, upon extended etching, the {111} facets decreased in area and eventually disappeared in the final stage of the etching (Fig. 2(f)). The Au microcrystals obtained at the intermediates stages exhibited two types of roughened surfaces, which are indicated as RS1 and RS2 in Fig. 2(b). The etching along the [100] direction produced RS1, while the corrugated surfaces that formed at the interface

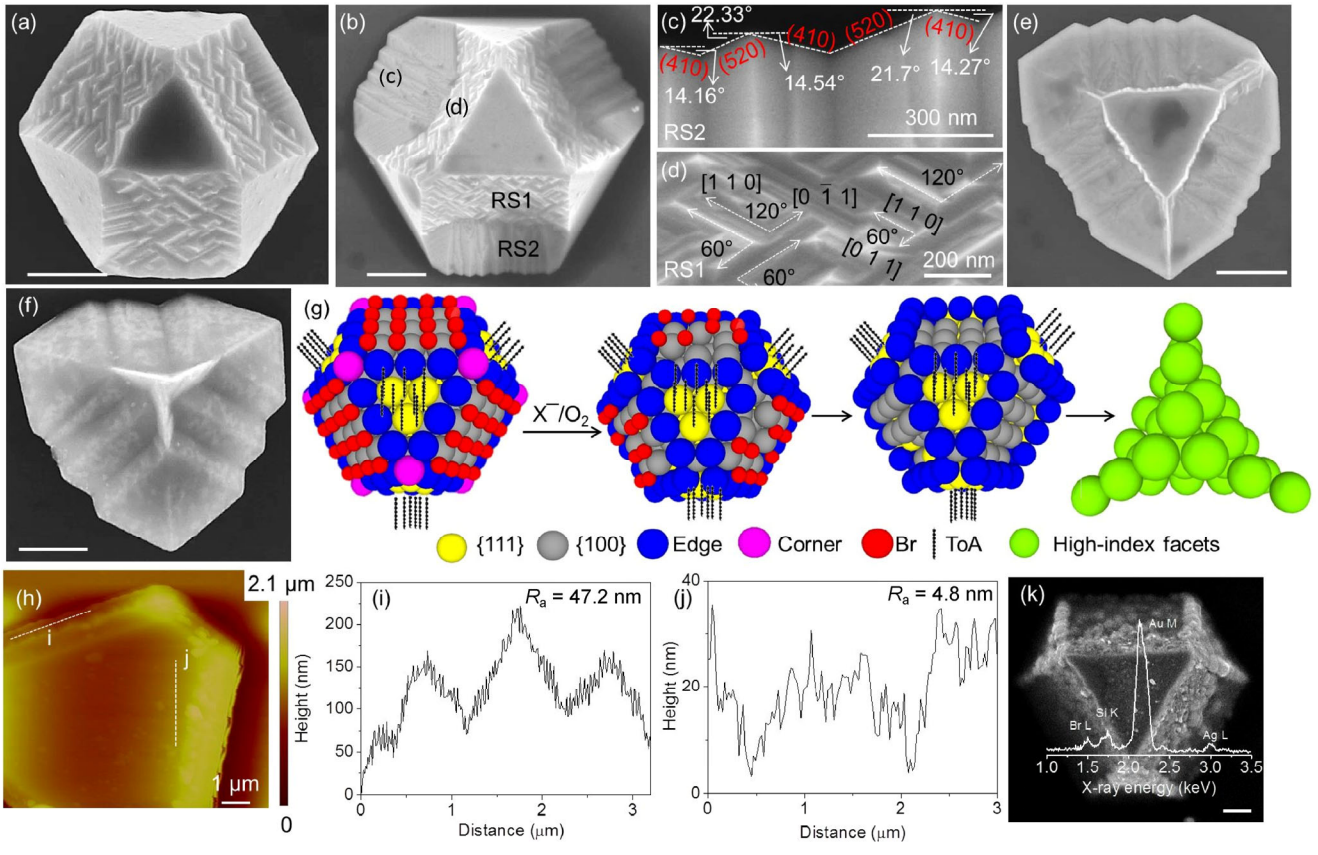

Figure 2 (a)–(f) SEM images of Au cuboctahedra at various stages of the {100}-facet etching. (g) Schematic showing selective etching of the {100} facet. (h) AFM topography of Au microcrystals. (i) and (j) Height profiles along the lines drawn in (h). The average roughness of the etched {100} and unetched {111} facets is 47.2 and 4.8 nm, respectively. (k) SEM image of the Au cuboctahedron after treatment with AgToABr in an Ar atmosphere. The corresponding EDS spectrum is shown at the top of (k). Scale bar represents 1 μm.

of {111} and {100} facets gave rise to RS2, which was parallel to the top and bottom {111} facets. The surface morphology differed considerably: RS2 exhibited well-defined corrugated steps (Fig. 2(c)), whereas RS1 exhibited an interconnected streak-like topography. The latter corresponds to mini {110} facets, as the angle between two adjacent mini facets is either 60° or 120° (Fig. 2(d)) [32]. On RS2, we observe two sets of angles between the pristine {100} facet and the corrugated features—14.34 ± 0.20° and 22.0 ± 0.3° (see Fig. 2(c))—which, according to the calculated angles of 14.04° and 21.8°, should correspond to the {410} and {520} facets, respectively [33]. It is interesting that the etching of the {100} facet can lead to such high-index facets. As the etching progresses along the [100] direction, RS1 diminishes (Fig. 2(e)), disappearing completely in the final product. As depicted in Fig. 2(f), the surface of the microcrystals is covered with only an RS2-type surface. Because of the preferential etching on the {100} facet, the surface roughness of the {100} facet is ~10 times higher than that of the {111} facets, and the heights of the corrugated steps are in the range of ~50–150 nm (see AFM data in Figs. 2(h) and 2(i)). The continued etching resulted in the formation of trigonal bipyramids covered with corrugated surfaces (Figs. 2(f) and 2(g) and Fig. S9 in the ESM). We propose the following etching mechanism on the basis of the aforementioned experimental observations, drawing from the literature for examples of the anisotropic etching of Pd nanocubes [7] and Ag octahedra [16]. The selective etching of the Au{100} facets involves four major steps: 1) the adsorption of tetraoctylammonium cation (ToA^+) on the {111} facets; 2) the oxidation of the atoms at the corners and edges; 3) the etching of the {100} facets; and 4) the redeposition of Au(III) or Au(I) on the etched {100} facets. The ToA^+ ion preferentially adsorbs on the {111} facets because of its higher adsorption energy [8]. To confirm that the Au{111} facets were covered with ToA^+ cations, Au microcrystals obtained from AuToABr were partially washed, and SEM imaging was performed. The Au{111} facets appeared to be covered with a thin organic layer. An EDS spectrum collected from the Au{111} indicated a weak C K signal that is attributed to the ToA^+ ligands adsorbed on the {111} surface. No Br^- was detected in the EDS spectrum collected from the Au{111} facets (Fig. S11 in the ESM). Interestingly, the SEM images reveal that the carbonaceous species was far less abundant on the Au{100} facets (see Fig. S11 in the ESM), which enabled selective etching. The long alkyl chain of the ToA^+ projected away from the Au{111} surface, making the surface hydrophobic [34]. Hence, a polar etchant such as O_2/Br^- may not able to attack the {111} facets. In addition, the higher surface energy of the Au{100} facet facilitates the selective etching of the {100} facet [4]. Atmospheric oxygen in combination with the halide anion available in the reaction medium (see Fig. S10 in the ESM) can etch gold to form soluble Au(I) or Au(III) complexes such as $(AuX_2)ToA$ (Au is in the +1 state) and $(AuX_4)ToA$ (Au is in the +3 state). The etching of the {100} facets begins at the corners because of the high reactivity due to the low coordination number and low bromide coverage [7]. As this process continues, the atoms on the {100} facets are etched away, and the Br^- ions are removed from the {100} facets (see the schematic in Fig. 2(g)). The etching of the {100} facets yields high-index facets that are more reactive compared with the low-index ones. The newly generated Au(III) or Au(I) complexes are reduced to Au(0) via thermal reduction and are deposited on the high-index facets (Eq. (1)).

$$(Au(III)/Au(I)X_{n=2\ or\ 4})ToA \xrightarrow{\Delta} Au(0) \quad (1)$$

As described in our previous work [35, 36], Ag(I) from AgToABr tends to deposit selectively on the Au{100} facets owing to the underpotential deposition (UPD), forming a monolayer or sub-monolayer of Ag(0). The Ag monolayer stabilizes the high-index facets [37]. However, the nature of the adsorption sites remains unclear. In the absence of Ag(I) (etching with ToABr alone), the etched surface was rather irregular (see Fig. S5 in the ESM). To examine the role of atmospheric oxygen in the etching process, thermolysis was performed in an Ar atmosphere. No etching occurred; instead, the thermolysis led to the formation of AgBr crystallites [38]. Thus, the AgBr was deposited on the cuboctahedra, as indicated by the EDS spectrum shown in Fig. 2(k) and elemental mapping (see Fig. S12 in the ESM). According to the aforementioned experiments, the plausible chemical equation for Au etching is as follows

$$Au + O_2 + X^- \longrightarrow Au(I)/Au(III) + O^{2-} \quad (2)$$

3.2 Etching of {111} facets

Similarly, the etching of {111} facets was attempted using a different etchant.

Fresh Au microcrystals were immersed in 1 mL of a 0.5 M $CuCl_2$ solution at 60 ℃, and the morphological changes were examined (Fig. 3). Compared with the {100} etching, in this case, the triangular {111} facets were etched, and the {100} facets were intact (Fig. 3(a)). The magnified image of Fig. 3(b) shows randomly distributed islands formed by the etching of the {111} facets, which is schematically illustrated in Fig. 3(c). In contrast to the Au{100} etching, the selective etching of the {111} facets did not yield corrugated facets. The etching of an Au cuboctahedron along the {111} facets produced a set of intermediate geometries, and the final product was a hexapod (Fig. 3(d)). To understand the etching process and identify the active etchant species, experiments were conducted. First, oxygen dissolved in a $CuCl_2$ solution was removed by adding Na_2SO_3, which is an O_2 scavenger [21]. Etching was then performed using this solution, and interestingly, no noticeable etching was observed, even after 12 h (see Fig. S13 in the ESM). This experimental observation confirms that oxygen is essential for etching Au surfaces. To address the role of the Cl^-, $CuSO_4$ was used instead of $CuCl_2$. Here also, no significant etching was observed (see Fig. S13 in the ESM). Similarly, the {111} facets were etched using NaCl instead of $CuCl_2$. Although etching was observed on the {111} facets, the extent of the etching was relatively low under the

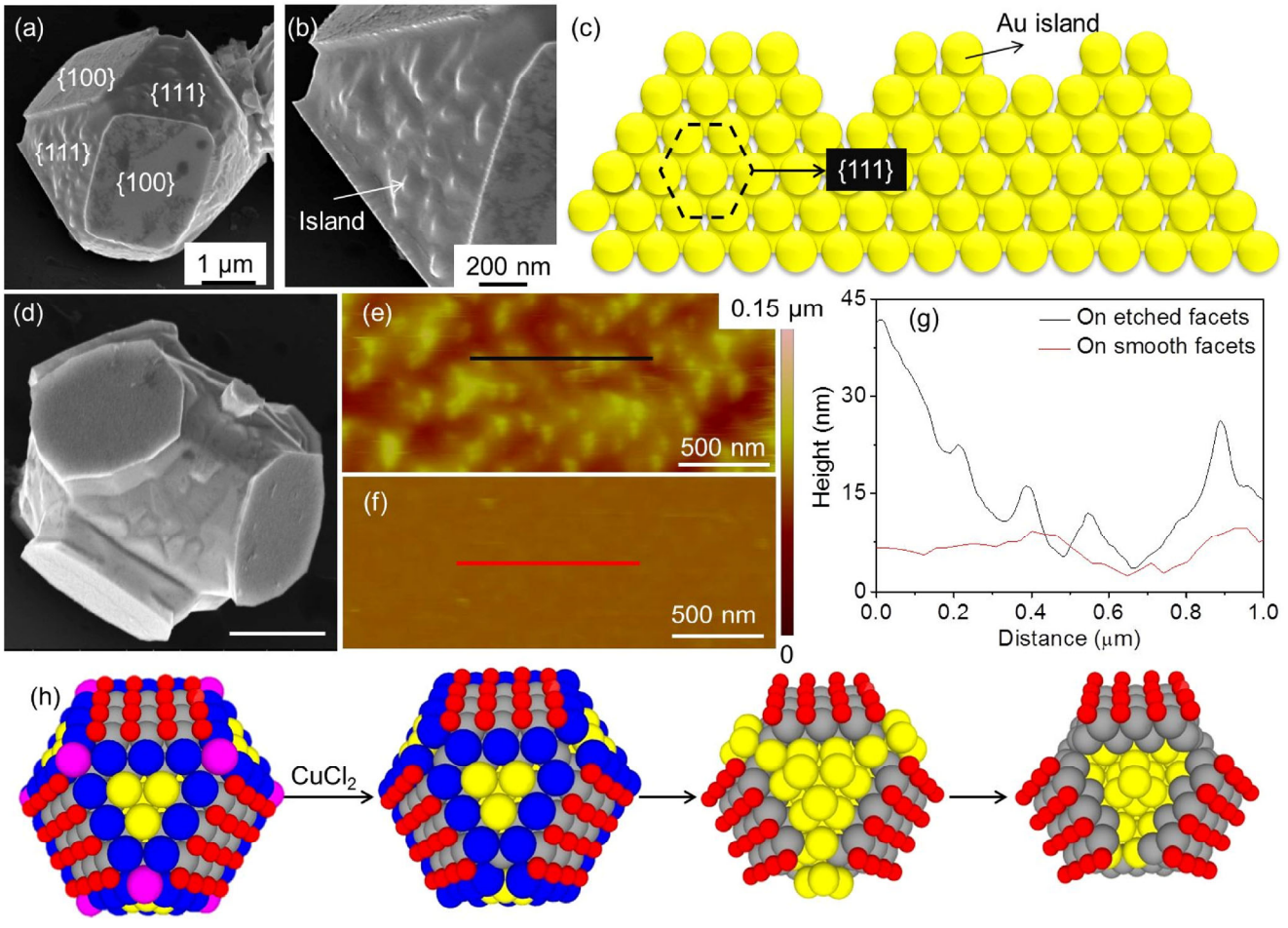

Figure 3 (a) and (b) SEM images of cuboctahedron obtained after treatment with 0.5 M $CuCl_2$. (c) Schematic of islands formed from {111} facets. (d) SEM images of a hexapod obtained by the selective etching of the Au{111} facets. (e) and (f) AFM topography images collected from various regions of a cuboctahedron. (g) Height profiles along the lines drawn in (e) and (f). (h) Plausible etching mechanism of {111} facets.

experimental conditions employed (see Fig. S6 in the ESM). Interesting dendrimeric etched patterns were observed, which may deserve a separate study. The milder action of the Na^+ is mainly due to its highly negative reduction potential (–2.71 eV). Cu(II), on the other hand, acts as a catalyst for the production of intermediates such as superoxide (O_2^-) that etch the Au surface [21, 39]. From the two aforementioned experiments, it is clear that Cu(II), Cl^- and O_2 are the active components of the etchant. It appears that the quaternary salts adsorbed on the {111} facets of the Au microcrystals (obtained from AuToABr) are removed during the toluene washing because of the high solubility of the ToABr in toluene (380 g/L) [40], whereas the Br^- may remain intact on the {100} facets owing to its poor solubility in toluene. Hence, the {111} facets are easily accessible for the etchant that is devoid of the capping agent. Similarly to the {100} etching, the {111} etching commenced at the corner and proceeded along the edges (see schematic Fig. 3(h)). The islands formed by the {111} etching were separated by ~100 nm, and their average height was ~10 nm (Figs. 3(e) and 3(g)). As the etching progressed, the roughness of the {111} etched facets (Fig. 3(e)) increased by an order of one compared with that of the {100} facets (see AFM data in Figs. 3(e)–3(g)). As previously mentioned, we observed several geometries in addition to cuboctahedra, such as truncated octahedra, hexagonal plates, triangles, and pentagonal nanowires (Fig. 4). In these cases also, the facets have smooth, with well-defined edges and corners prior to the etching (Figs. 4(a)–4(c), 4(h) and 4(m)). Similarly to cuboctahedra, cuboctahedron derivatives exhibit the selective etching of the {100} facets with AgToABr (Figs. 4(d)–4(f), 4(i)–4(k), and 4(n)–4(p)). Continued etching along the [100] direction caused the formation of trigonal bipyramidal microcrystals covered with corrugated surfaces. In the case of Au nanowires, the selective etching of the {100} facets produced corrugated pentagonal nanowires (Figs. 4(n) and 4(o)). However, the tips of {111} were unaffected by the etchant (Fig. 4(p)). On the other hand, the selective etching of the {111} facet was observed with $CuCl_2$ (Figs. 4(g), 4(l), and 4(q)–4(s)). Notably, the anisotropic etching of the Au{100} and Au{111} facets is purely facet-dependent and is independent of the geometry and size of the Au microcrystals. The process is substantiated by growing Au crystals ~300 nm in size and etching the {100} and {111} facets using AgToABr and $CuCl_2$, respectively (see Fig. S14 in the ESM). This process should be applicable for smaller sizes, although the imaging becomes more complex. In the present study, which involved large microcrystals, the finer steps of the etching are clarified, and the surface crystallography of the etched facets is evident. As evidenced by the aforementioned cases, all the intermediate stages of the selective etching of Au microcrystals were identified using ordinary electron microscopy, which is simply impossible with nanoparticles owing to their small dimensions. These larger dimensions are handy and attractive not only in the context of the facet selective etching phenomenon but also because of the emergence of crystallographically well-defined nanocorrugated surfaces over large areas. For instance, the selective etching of the {100} facets of penta-twinned microrods produced nanocorrugated Au microrods, while there were no changes in the length of rods. Usually, such corrugated nanowires are obtained only using sophisticated lithography techniques [41]. To our knowledge, this is the first report of the successful anisotropic etching of Au microcrystals. Nanocorrugated surfaces are interesting with regard to the surface plasmon polaritons and their interaction with light (see Fig. S15 in the ESM) [42]. In the current literature, the facet selective etching of metals is known only for the {100} facets of Ag and Pd nanocrystals.

4 Conclusions

We investigated for the first time the anisotropic etching of Au in the form of microcrystals. Specific geometries belonging to a cuboctahedron, truncated octahedron, hexagon, triangle, and pentagonal rod were observed, each a few tens of microns in size and enclosed by {111} and {100} facets. Gold etching was performed in atmospheric O_2 in the presence of halides. Selective etching of the {100} facets occurred as the ToA^+ ions present in the reaction medium selectively capped the {111} facets. Similarly, the {100} facets were protected by the adsorbed Br^- ions while the {111}

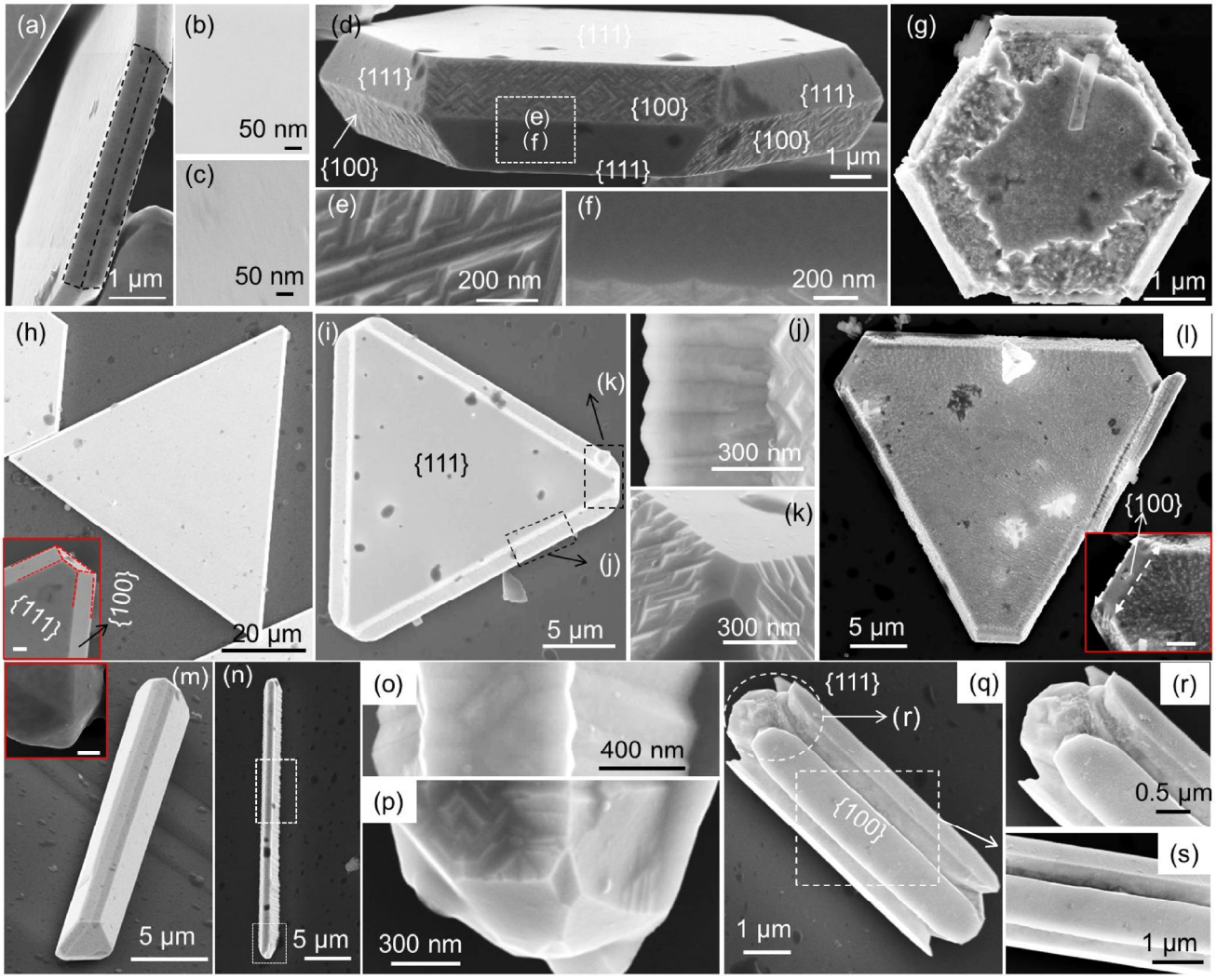

Figure 4 SEM images of Au hexagons, triangles, and microrods before etching ((a)–(c), (h), and (m)), after selective {100} etching ((d)–(f), (i)–(k), and (n)–(p)), and after {111} etching ((g), (l), and (q)–(s)), respectively. Scale bar represents 300 nm.

facets were etched. Trigonal bipyramids and hexapods were the final products obtained by the selective etching of the {100} and {111} facets, respectively. In both cases, the etching began at the corners and then spread toward the edges. Complete etching produced corrugated facets that were assigned to high indices. The anisotropic etching of the microcrystals was remarkable not only for producing various interesting shapes but also for creating high-index facets over a large surface area (hundreds of μm^2). More importantly, we observed that the selective etching depended only on the crystallography of the facets and not on the specific geometry of the microcrystal. Owing to the nanocorrugations, the etched surfaces exhibited enhanced Raman signals of an analyte, whereas the smooth surfaces exhibited no such enhancement.

Acknowledgements

The authors thank Nanomission DST, India for generous support. The authors thank Prof. C. N. R. Rao for his constant encouragement. We thank Dr. Basavaraja S, Mr. Vasu Deva and Dr. Venkata Srinu Bhadram for AFM, TGA and Raman measurements. G. M. thanks CSIR, India for financial assistance.

Electronic Supplementary Material: Supplementary material (summary of literature showing the conditions

have been adopted for Au nanoparticles etching, SEM images of Au microcrystals pre-etching, after etching with $FeCl_3$, NaCl, H_2O_2 and ToABr. Elemental analysis and Raman spectroscopy measurements) is available in the online version of this article at http://dx.doi.org/10.1007/s12274-015-0797-8.

References

[1] Seidel, H.; Csepregi, L.; Heuberger, A.; Baumgärtel, H. Anisotropic etching of crystalline silicon in alkaline solutions: I . Orientation dependence and behavior of passivation layers. *J. Electrochem. Soc.* **1990**, *137*, 3612–3626.

[2] Leancu, R.; Moldovan, N.; Csepregi, L.; Lang, W. Anisotropic etching of germanium. *Sensor. Actuat. A-Phys* **1995**, *46*, 35–37.

[3] Ng, H. M.; Weimann, N. G.; Chowdhury, A. GaN nanotip pyramids formed by anisotropic etching. *J. Appl. Phys.* **2003**, *94*, 650–653.

[4] Kan, C. X.; Wang, C. S.; Li, H. C.; Qi, J. S.; Zhu, J. J.; Li, Z. S.; Shi, D. N. Gold microplates with well-defined shapes. *Small* **2010**, *6*, 1768–1775.

[5] Magnussen, O. M. Ordered anion adlayers on metal electrode surfaces. *Chem. Rev.* **2002**, *102*, 679–726.

[6] Kilin, D. S.; Prezhdo, O. V.; Xia, Y. N. Shape-controlled synthesis of silver nanoparticles: *Ab initio* study of preferential surface coordination with citric acid. *Chem. Phys. Lett.* **2008**, *458*, 113–116.

[7] Liu, M. C.; Zheng, Y. Q.; Zhang, L.; Guo, L. J.; Xia, Y. N. Transformation of Pd nanocubes into octahedra with controlled sizes by maneuvering the rates of etching and regrowth. *J. Am. Chem. Soc.* **2013**, *135*, 11752–11755.

[8] Meena, S. K.; Sulpizi, M. Understanding the microscopic origin of gold nanoparticle anisotropic growth from molecular dynamics simulations. *Langmuir* **2013**, *29*, 14954–14961.

[9] Long, R.; Zhou, S.; Wiley, B. J.; Xiong, Y. J. Oxidative etching for controlled synthesis of metal nanocrystals: Atomic addition and subtraction. *Chem. Soc. Rev.* **2014**, *43*, 6288–6310.

[10] Kou, X. S.; Ni, W. H.; Tsung, C.-K.; Chan, K.; Lin, H.-Q.; Stucky, G. D.; Wang, J. F. Growth of gold bipyramids with improved yield and their curvature-directed oxidation. *Small* **2007**, *3*, 2103–2113.

[11] Rodríguez-Fernandez, J.; Perez-Juste, J.; Mulvaney, P.; Liz-Marzán, L. M. Spatially-directed oxidation of gold nanoparticles by Au(III)−CTAB complexes. *J. Phys. Chem. B* **2005**, *109*, 14257–14261.

[12] Zou, R. X.; Guo, X.; Yang, J.; Li, D. D.; Peng, F.; Zhang, L.; Wang, H. J.; Yu, H. Selective etching of gold nanorods by ferric chloride at room temperature. *CrystEngComm* **2009**, *11*, 2797–2803.

[13] Chen, Z. P.; Liu, R. L.; Wang, S. S.; Qu, C. L.; Chen, L. X.; Wang, Z. Colorimetric sensing of copper(Ⅱ) based on catalytic etching of gold nanorods. *RSC Adv.* **2013**, *3*, 13318–13323.

[14] Wen, T.; Zhang, H.; Tang, X. P.; Chu, W. G.; Liu, W. Q.; Ji, Y. L.; Hu, Z. J.; Hou, S.; Hu, X. N.; Wu, X. C. Copper ion assisted reshaping and etching of gold nanorods: Mechanism studies and applications. *J. Phys. Chem. C* **2013**, *117*, 25769–25777.

[15] Dai, D. G.; Xu, D.; Cheng, X. D.; He, Y. Direct imaging of single gold nanoparticle etching: Sensitive detection of lead ions. *Anal. Methods* **2014**, *6*, 4507–4511.

[16] Mulvihill, M. J.; Ling, X. Y.; Henzie, J.; Yang, P. D. Anisotropic etching of silver nanoparticles for plasmonic structures capable of single-particle SERS. *J. Am. Chem. Soc.* **2009**, *132*, 268–274.

[17] Zhang, J. F.; Feng, C.; Deng, Y. D.; Liu, L.; Wu, Y. T.; Shen, B.; Zhong, C.; Hu, W. B. Shape-controlled synthesis of palladium single-crystalline nanoparticles: The effect of hcl oxidative etching and facet-dependent catalytic properties. *Chem. Mater.* **2014**, *26*, 1213–1218.

[18] Jana, N. R.; Gearheart, L.; Obare, S. O.; Murphy, C. J. Anisotropic chemical reactivity of gold spheroids and nanorods. *Langmuir* **2002**, *18*, 922–927.

[19] Shao, J. R.; Josephs, E. A.; Lee, C.; Lopez, A.; Ye, T. Electrochemical etching of gold within nanoshaved self-assembled monolayers. *ACS Nano* **2013**, *7*, 5421–5429.

[20] Ye, S.; Ishibashi, C.; Uosaki, K. Anisotropic dissolution of an Au(111) electrode in perchloric acid solution containing chloride anion investigated by in situ STM-The important role of adsorbed chloride anion. *Langmuir* **1999**, *15*, 807–812.

[21] Sreeprasad, T. S.; Samal, A. K.; Pradeep, T. Body- or tip-controlled reactivity of gold nanorods and their conversion to particles through other anisotropic structures. *Langmuir* **2007**, *23*, 9463–9471.

[22] Saa, L.; Coronado-Puchau, M.; Pavlov, V.; Liz-Marzan, L. M. Enzymatic etching of gold nanorods by horseradish peroxidase and application to blood glucose detection. *Nanoscale* **2014**, *6*, 7405–7409.

[23] Tsung, C. K.; Kou, X. S.; Shi, Q. H.; Zhang, J. P.; Yeung, M. H.; Wang, J. F.; Stucky, G. D. Selective shortening of single-crystalline gold nanorods by mild oxidation. *J. Am. Chem. Soc.* **2006**, *128*, 5352–5353.

[24] Fan, N. N.; Yang, Y.; Wang, W. F.; Zhang, L. J.; Chen, W.; Zou, C.; Huang, S. M. Selective etching induces selective growth and controlled formation of various platinum nano-structures by modifying seed surface free energy. *ACS Nano* **2012**, *6*, 4072–4082.

[25] Radha, B.; Arif, M.; Datta, R.; Kundu, T. K.; Kulkarni, G. U. Movable Au microplates as fluorescence enhancing substrates for live cells. *Nano Res.* **2010**, *3*, 738–747.

[26] Radha, B.; Kulkarni, G. U. A real time microscopy study of the growth of giant au microplates. *Cryst. Growth Des.* **2011**, *11*, 320–327.

[27] Zhang, Z.-C.; Nosheen, F.; Zhang, J.-C.; Yang, Y.; Wang, P.-P.; Zhuang, J.; Wang, X. Growth of concave polyhedral Pd nanocrystals with 32 facets through *in situ* facet-selective etching. *ChemSusChem* **2013**, *6*, 1893–1897.

[28] Levinstein, H. J.; Robinson, W. H. Etch pits at dislocations in silver single crystals. *J. Appl. Phys.* **1962**, *33*, 3149–3152.

[29] Radha, B.; Kiruthika, S.; Kulkarni, G. U. Metal anion–alkyl ammonium complexes as direct write precursors to produce nanopatterns of metals, nitrides, oxides, sulfides, and alloys. *J. Am. Chem. Soc.* **2011**, *133*, 12706–12713.

[30] Gilroy, K. D.; Farzinpour, P.; Sundar, A.; Tan, T.; Hughes, R. A.; Neretina, S. Substrate-based galvanic replacement reactions carried out on heteroepitaxially formed silver templates. *Nano Res.* **2013**, *6*, 418–428.

[31] Pileni, M. P. Supra- and nanocrystallinities: A new scientific adventure. *J. Phys.: Condens. Matter* **2011**, *23*, 503102.

[32] Personick, M. L.; Langille, M. R.; Zhang, J.; Harris, N.; Schatz, G. C.; Mirkin, C. A. Synthesis and isolation of {110}-faceted gold bipyramids and rhombic dodecahedra. *J. Am. Chem. Soc.* **2011**, *133*, 6170–6173.

[33] Zhang, J. A.; Langille, M. R.; Personick, M. L.; Zhang, K.; Li, S. Y.; Mirkin, C. A. Concave cubic gold nanocrystals with high-index facets. *J. Am. Chem. Soc.* **2010**, *132*, 14012–14014.

[34] Tsao, Y. H.; Yang, S. X.; Evans, D. F.; Wennerstroem, H. Interactions between hydrophobic surfaces. Dependence on temperature and alkyl chain length. *Langmuir* **1991**, *7*, 3154–3159.

[35] Mettela, G.; Boya, R.; Singh, D.; Kumar, G. V. P.; Kulkarni, G. U. Highly tapered pentagonal bipyramidal Au microcrystals with high index faceted corrugation: Synthesis and optical properties. *Sci. Rep.* **2013**, *3*, 1793.

[36] Mettela, G.; Bhogra, M.; Waghmare, U. V.; Kulkarni, G. U. Ambient stable tetragonal and orthorhombic phases in penta-twinned bipyramidal Au microcrystals. *J. Am. Chem. Soc.* **2015**, *137*, 3024–3030.

[37] Personick, M. L.; Langille, M. R.; Zhang, J.; Mirkin, C. A. Shape control of gold nanoparticles by silver underpotential deposition. *Nano Lett.* **2011**, *11*, 3394–3398.

[38] Mettela, G.; Siddhanta, S.; Narayana, C.; Kulkarni, G. U. Nanocrystalline Ag microflowers as a versatile SERS platform. *Nanoscale* **2014**, *6*, 7480–7488.

[39] Zhang, Z. Y.; Chen, Z. P.; Pan, D. W.; Chen, L. X. Fenton-like reaction-mediated etching of gold nanorods for visual detection of Co^{2+}. *Langmuir* **2015**, *31*, 643–650.

[40] Luthra, S. S.; Yang, X. J.; dos Santos, L. M. F.; White, L. S.; Livingston, A. G. Phase-transfer catalyst separation and re-use by solvent resistant nanofiltration membranes. *Chem. Commun.* **2001**, 1468–1469.

[41] Lindquist, N. C.; Nagpal, P.; Lesuffleur, A.; Norris, D. J.; Oh, S.-H. Three-dimensional plasmonic nanofocusing. *Nano Lett.* **2010**, *10*, 1369–1373.

[42] Brolo, A. G.; Irish, D. E.; Szymanski, G.; Lipkowski, J. Relationship between SERS intensity and both surface coverage and morphology for pyrazine adsorbed on a polycrystalline gold electrode. *Langmuir* **1998**, *14*, 517–527.